

# Collective states and shape competition in $^{126}\text{Te}^*$

Liu-Chun He (何鑾春)<sup>1</sup> Yun Zheng (郑云)<sup>2;1)</sup> Li-Hua Zhu (竺礼华)<sup>1,3;2)</sup> Hai-Liang Ma (马海亮)<sup>2</sup>  
 Xiao-Guang Wu (吴晓光)<sup>2</sup> Chuang-Ye He (贺创业)<sup>2</sup> Guang-Sheng Li (李广生)<sup>2</sup>  
 Lie-Lin Wang (王列林)<sup>2,4</sup> Xin Hao (郝昕)<sup>2,3</sup> Ying Liu (刘颖)<sup>2</sup> Xue-Qin Li (李雪琴)<sup>2</sup>  
 Bo Pan (潘波)<sup>2</sup> Zhong-Yu Li (李忠宇)<sup>5</sup> Huai-Bo Ding (丁怀博)<sup>6</sup>

<sup>1</sup> School of Physics and Nuclear Energy Engineering, Beihang University, Beijing 100191, China

<sup>2</sup> China Institute of Atomic Energy, Beijing 102413, China

<sup>3</sup> Faculty of Science, Shenzhen University, Shenzhen 518060, China

<sup>4</sup> Fundamental Science on Nuclear Wastes and Environmental Safety Laboratory, Mianyang 621010, China

<sup>5</sup> School of Physics, Peking University, Beijing 100871, China

<sup>6</sup> Department of Physics, Tsinghua University, Beijing 100084, China

**Abstract:** High-spin states in  $^{126}\text{Te}$  have been investigated by using in-beam  $\gamma$  ray spectroscopy with the  $^{124}\text{Sn}(^7\text{Li}, 1\text{p}4\text{n})^{126}\text{Te}$  reaction at a beam energy of 48 MeV. The previously known level scheme has been enriched, and a new negative-parity sequence has been established. The yrast positive-parity band shows a shape change between triaxial shape and collective oblate shape as a function of spin. In particular, three competitive minima appear in the potential energy surface for the  $I^\pi = 8^+$  states, with one aligned state at  $\gamma = -120^\circ$  and two triaxial states at  $\gamma \sim 30^\circ$  and  $-45^\circ$ , respectively. The signature splitting behavior of the negative-parity band is discussed. The shape change with increasing angular momentum and the signature splitting can be interpreted well in terms of the Cranked Nilsson-Strutinsky-Bogoliubov and Cranked Nilsson-Strutinsky model calculations.

**Keywords:** shape competition, signature splitting, collective states

**PACS:** 21.10.Re, 27.60.+j, 21.60.Ev      **DOI:** 10.1088/1674-1137/41/4/044003

## 1 Introduction

The Te isotopes, two protons beyond the closed  $Z = 50$  shell, lie in the transitional region between the spherical nuclei at  $Z = 50$  and deformed La and Ce nuclei. In this  $A \sim 125$  mass region, the proton Fermi surface lies in the lower part of the  $h_{11/2}$  orbitals, which favors a prolate shape, while neutrons occupy medium- to high- $\Omega$  orbitals of the  $h_{11/2}$  subshell, which drive the shape towards oblate [1]. The deformation-driving properties of neutrons and protons are therefore conflicting and a given nucleus may have either a prolate, oblate or triaxial shape depending on the configuration [2, 3]. Furthermore, shape changes as a function of spin are expected in these nuclei due to the opposite shape-driving tendencies of protons and neutrons. Shape change arises from successive alignments of nucleons and has been investigated up to high spin in several nuclei of the mass  $A \sim 125$  region [1, 2, 4–6]. It is worth pointing out that strong shape-polarization effects due to two quasiparticles has

been predicted in this mass region by Xu et al. [7]. In addition, in this mass region, the valence neutrons filled near the neutron Fermi surface result in a drive to negative  $\gamma$  (i.e. a more collective oblate shape). The effects are seen experimentally as signature splitting in the transition energies [8, 9].

The low-lying states of  $^{126}\text{Te}$  have been investigated by a variety of experiments, i.e.,  $(n, n'\gamma)$  [10],  $(n, \gamma)$  [11],  $(d, p)$ ,  $(d, ^3\text{He})$ ,  $(d, d')$  [12], and  $(\alpha, 2n)$  [13] reactions. High spin levels have also been established by Zhang et al [14] with the multi-nucleon transfer reaction  $^{130}\text{Te} + ^{64}\text{Ni}$ . It should be noted that a new level scheme was reported by Astier et al [15] with two fusion fission reactions  $^{12}\text{C} + ^{238}\text{U}$  and  $^{18}\text{O} + ^{208}\text{Pb}$  while this paper was being prepared.

In this article, we report the experimental results of heavy-ion fusion-evaporation reaction and theoretical studies on the high spin structures in  $^{126}\text{Te}$ . Several new levels and a new sequence have been identified and the previous level scheme has been enriched.

Received 17 October 2016, Revised 7 December 2016

\* Supported by National Natural Science Foundation of China (11575018, 11375023, 11305269, 11375267, 11405274, 11205245, 10927507, 10975191, 11075214, 11175259, 11205068)

1) E-mail: zhengyun@ciae.ac.cn

2) E-mail: zhulh@buaa.edu.cn

©2017 Chinese Physical Society and the Institute of High Energy Physics of the Chinese Academy of Sciences and the Institute of Modern Physics of the Chinese Academy of Sciences and IOP Publishing Ltd

The major aim of the present work is to investigate the shape change as a function of spin. In addition, a signature splitting in the energy levels of the negative-parity band was observed. The theoretical interpretation of level structure in  $^{126}\text{Te}$  is performed in the framework of the cranked Nilsson-Strutinsky-Bogoliubov (CNSB) model and cranked Nilsson-Strutinsky (CNS) model.

## 2 Experimental methods and results

Excited states in the nucleus  $^{126}\text{Te}$  were populated via the heavy-ion fusion-evaporation reaction  $^{124}\text{Sn}(^7\text{Li}, 1\text{p}4\text{n})^{126}\text{Te}$ . The  $^7\text{Li}$  beam, with an energy of 48 MeV, was delivered by the HI-13 tandem accelerator at the China Institute of Atomic Energy. The target was an enriched self-supporting  $^{124}\text{Sn}$  ( $(97.5 \pm 0.2)\%$ ) metallic foil of 4.6 mg/cm<sup>2</sup> thickness. The  $\gamma$  rays emitted from the evaporation residues were detected with a multi detector array consisting of 12 BGO-Compton-suppressed HPGe detectors, whose energy resolutions were about 2.0–2.5 keV at 1.33 MeV, and two planar HPGe detectors with energy resolutions of 0.6–0.7 keV at 121.78 keV. All HPGe detectors were calibrated for energy and efficiency using the standard energy calibration  $\gamma$  lines from the

decay of  $^{133}\text{Ba}$  and  $^{152}\text{Eu}$  radioactive sources. A total of  $9.4 \times 10^7 \gamma\gamma$  coincidence events were accumulated in event-by-event mode. After energy calibration and gain matching for different detectors, the recorded  $\gamma\gamma$  coincidence events were sorted into a two-dimensional  $E_\gamma$ - $E_\gamma$  symmetric matrix, and then analyzed using the software package RADWARE [16].

To obtain information on the multipolarity of  $\gamma$  rays, the ratios of directional correlation of oriented states (DCO) have been analyzed from an asymmetric DCO matrix created by sorting the data with the detectors at  $\sim \pm 40^\circ$  on one axis and the detectors at  $\sim 90^\circ$  on the other axis. The DCO ratios, defined as  $R_{\text{DCO}} = I_\gamma(40^\circ)/I_\gamma(90^\circ)$ , were extracted from the  $\gamma$  ray intensities  $I_\gamma(40^\circ)$  and  $I_\gamma(90^\circ)$  in the coincidence spectra obtained by setting the same gates on the  $90^\circ$  and  $40^\circ$  axis of the DCO matrix, respectively. In the present experiment, when the gate is set on a quadrupole transition the  $R_{\text{DCO}}$  value is around 1.0 for stretched  $E2$  transitions and less than 0.7 for stretched dipole transitions. Similarly, with the gate on a dipole transition, the  $R_{\text{DCO}}$  value is close to 1.6 and 1.0 for quadrupole and dipole transitions respectively.

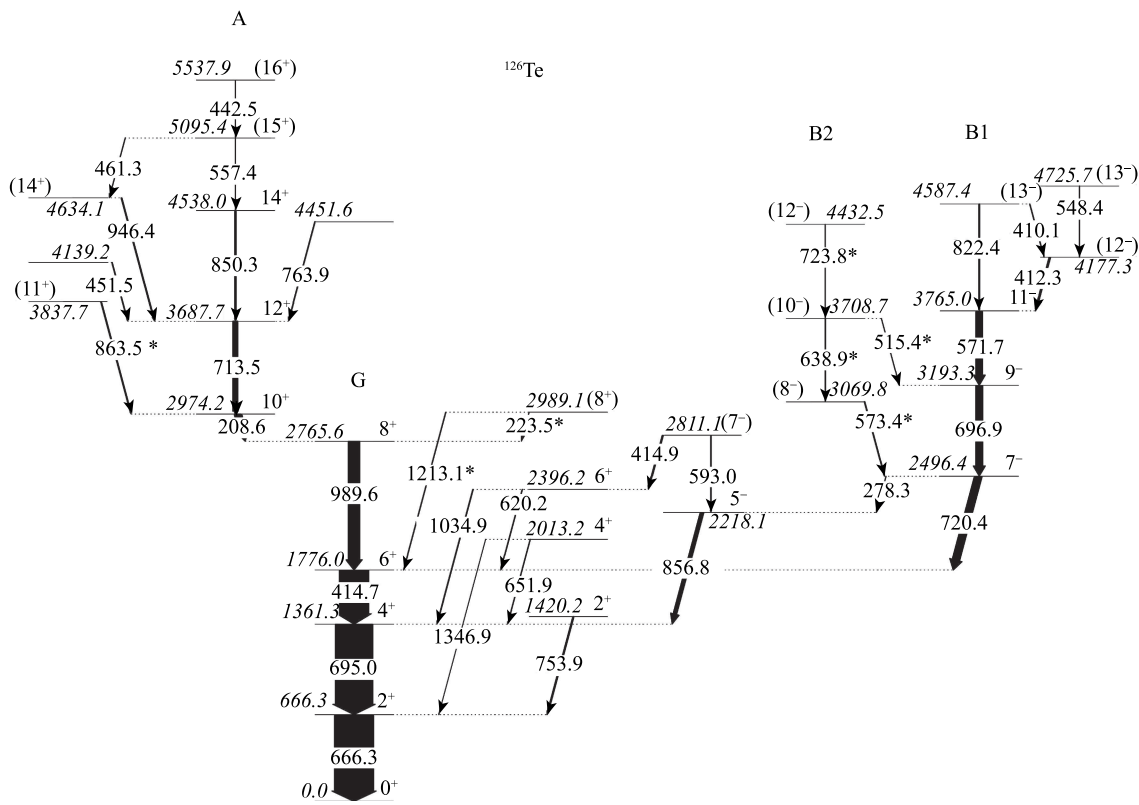


Fig. 1. The level scheme of  $^{126}\text{Te}$  established from the present work. New  $\gamma$  rays are marked with asterisks.

The enriched level scheme of  $^{126}\text{Te}$  deduced from the present work is shown in Fig. 1. The placement of  $\gamma$  rays in the level scheme is based on the  $\gamma$ - $\gamma$  coincidence relations and  $\gamma$ -ray intensities. Spin and parity assignments are on the basis of  $\gamma$ - $\gamma$  directional correlations and deexcitation modes. The energies, DCO ratios, multipoles of  $\gamma$  rays and the spin and parity  $I^\pi$  assignments of levels are summarized in Table 1. Compared with

the results reported in Refs. [14, 15], the level scheme of  $^{126}\text{Te}$  has been modified and enriched in the present work. Seven new  $\gamma$  rays have been identified and placed in the present level scheme. Particularly, a new negative-parity sequence, labeled with B2 on the top of the sequence in Fig. 1, as well as three cross-link transitions have been identified. Some detailed experimental results are given below.

Table 1. Energies, relative intensities, DCO ratios, and initial and final state spin-parities of  $\gamma$  ray transitions assigned to  $^{126}\text{Te}$  in the present work.

$E_\gamma$ (keV) <sup>a</sup>	$I_\gamma^b$	$E_i \rightarrow E_f$ (keV) <sup>c</sup>	$R_{\text{DCO}}(D)^d$	$R_{\text{DCO}}(Q)^e$	$J_i^\pi \rightarrow J_f^\pi$
208.6	17.1(2)	2974.2→2765.6		1.26(7)	$10^+ \rightarrow 8^+$
223.5	0.6(1)	2989.1→2765.6			$(8^+) \rightarrow 8^+$
278.3	0.7(1)	2496.4→2218.1	1.4(5)		$7^- \rightarrow 5^-$
410.1	1.2(1)	4587.4→4177.3		0.52(19)	$(13^-) \rightarrow (12^-)$
412.3	4.2(2)	4177.3→3765.0		0.60(12)	$(12^-) \rightarrow 11^-$
414.7	74.2(8)	1776.0→1361.3	1.81(7)	1.07(2)	$6^+ \rightarrow 4^+$
414.9	3.2(2)	2811.1→2396.2			$(7^-) \rightarrow 6^+$
442.5	0.8(1)	5537.9→5095.4	1.1(5)	0.48(17)	$(16^+) \rightarrow (15^+)$
451.5	1.7(5)	4139.2→3687.7			
461.3	0.8(1)	5095.4→4634.1		0.63(22)	$(15^+) \rightarrow (14^+)$
515.4	0.6(1)	3708.7→3193.3		0.47(23)	$(10^-) \rightarrow 9^-$
548.4	1.7(3)	4725.7→4177.3		0.49(10)	$(13^-) \rightarrow (12^-)$
557.4	0.9(4)	5095.4→4538.0		0.47(12)	$(15^+) \rightarrow 14^+$
571.7	17.3(9)	3765.0→3193.3		1.05(9)	$11^- \rightarrow 9^-$
573.4	1.9(3)	3069.8→2496.4		0.48(17)	$(8^-) \rightarrow 7^-$
593.0	1.7(1)	2811.1→2218.1	1.61(20)		$(7^-) \rightarrow 5^-$
620.2	1.3(1)	2396.2→1776.0		1.5(6)	$6^+ \rightarrow 6^+$
638.9	1.1(5)	3708.7→3069.8	2.2(8)		$(10^-) \rightarrow (8^-)$
651.9	1.1(1)	2013.2→1361.3		1.8(6)	$4^+ \rightarrow 4^+$
666.3	100.0	666.3→0.0	1.69(15)	1.05(4)	$2^+ \rightarrow 0^+$
695.0	95.4(7)	1361.3→666.3		1.04(3)	$4^+ \rightarrow 2^+$
696.9	17.9(9)	3193.3→2496.4		1.51(24)	$9^- \rightarrow 7^-$
713.5	12.8(2)	3687.7→2974.2		1.09(5)	$12^+ \rightarrow 10^+$
720.4	19.6(2)	2496.4→1776.0		0.48(4)	$7^- \rightarrow 6^+$
723.8	0.7(2)	4432.5→3708.7		0.9(5)	$(12^-) \rightarrow (10^-)$
753.9	3.3(1)	1420.2→666.3		1.8(4)	$2^+ \rightarrow 2^+$
763.9	1.5(1)	4451.6→3687.7			
822.4	2.9(1)	4587.4→3765.0		0.98(14)	$(13^-) \rightarrow 11^-$
850.3	4.2(1)	4538.0→3687.7		0.99(12)	$14^+ \rightarrow 12^+$
856.8	9.4(2)	2218.1→1361.3		0.53(4)	$5^- \rightarrow 4^+$
863.5	2.5(1)	3837.7→2974.2		0.67(9)	$(11^+) \rightarrow 10^+$
946.4	2.5(1)	4634.1→3687.7		0.84(15)	$(14^+) \rightarrow 12^+$
989.6	29.2(3)	2765.6→1776.0		0.88(18)	$8^+ \rightarrow 6^+$
1034.9	1.6(1)	2396.2→1361.3		1.2(22)	$6^+ \rightarrow 4^+$
1213.1	1.1(1)	2989.1→1776.0		1.0(5)	$(8^+) \rightarrow 6^+$
1346.9	0.3(5)	2013.2→666.3		0.9(4)	$4^+ \rightarrow 2^+$

<sup>a</sup>Uncertainties are between 0.2 and 0.5 keV depending upon their intensity.

<sup>b</sup>Intensities are normalized to the 666.3 keV transition with  $I_\gamma=100$ .

<sup>c</sup>Excitation energies of initial  $E_i$  and final  $E_f$  states.

<sup>d</sup>DCO ratios gated by dipole transitions.

<sup>e</sup>DCO ratios gated by quadrupole transitions.

<sup>f</sup>Proposed spin and parity assignments to the initial  $J_i^\pi$  and final  $J_f^\pi$  levels.

For the positive-parity part of the level scheme, most of the  $\gamma$  rays reported in the previous works [14, 15] have been confirmed in the present work, and four new  $\gamma$  rays have been identified. The  $I^\pi = (16^+)$  level at 5.69 MeV reported in Ref. [15] has not been observed in the present work. A new ( $8^+$ ) level at 2989.1 keV has been identified, which feeds into the  $6^+$  and  $8^+$  yrast states through 1213.1 and 223.5 keV  $\gamma$  rays, respectively. The  $R_{DCO}$  values of 1213.1-keV  $\gamma$  transition suggests a quadrupole character of  $\Delta I = 2$ , and therefore  $I^\pi = (8^+)$  was tentatively assigned to the 2989.1 keV level. Another newly identified 3837.7 keV level feeds into the yrast  $10^+$  state. The spin of this state is deduced from the  $R_{DCO}$  value of 863.5 keV  $\gamma$  ray, which suggests a dipole character of  $\Delta I = 1$ . As an example, Fig. 2 shows the coincidence

spectra gated by the 666.3, 989.6, and 208.6 keV  $\gamma$  rays, respectively, of positive-parity structure. In Fig. 2 (a), most the previously known  $\gamma$  rays of the bands G and A as well as the newly identified 863.5 and 1213.1 keV  $\gamma$  rays can be clearly seen. Another newly identified 223.5-keV  $\gamma$  ray can be clearly seen from the  $\gamma$ -ray coincidence spectrum gated on the 989.6 keV  $\gamma$  ray, as shown in Fig. 2 (b). In addition, Fig. 2 (c) shows the coincidence spectrum gated by the 208.6 keV  $\gamma$  ray, where all of the previous known  $\gamma$  rays of the bands G and A as well as the newly identified 863.5 keV  $\gamma$  ray can be clearly seen. It should be noted that the peaks marked with asterisks are contaminants of the strongly populated by-products (such as  $^{125,126,127}\text{I}$  and  $^{125}\text{Te}$ ) from the reaction, as shown in Figs. 2 and 3.

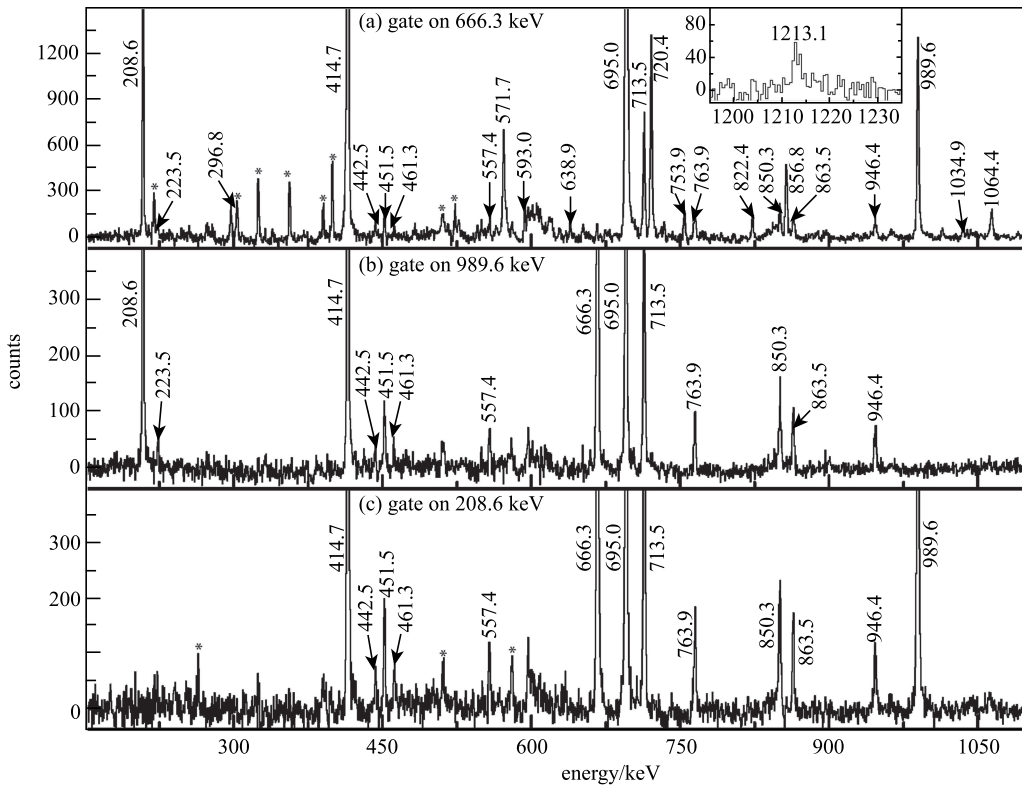


Fig. 2. Representative  $\gamma$ - $\gamma$  coincidence spectra gated on (a) 666.3, (b) 989.6, and (c) 208.6 keV transitions. The main coincidence  $\gamma$  rays are labeled with their energies in keV, while the peaks marked with asterisks are contaminants of the by-products (such as  $^{126}\text{I}$  and  $^{125}\text{Te}$ ) from the reaction.

Band B1 is an yrare band with negative parity based on the  $7^-$  state at 2496.4 keV. This band includes two sequences of  $\Delta I = 2$  transitions with weak  $\Delta I = 1$  cross-link transitions, and it decays out mainly from the band-head into the ground band G via 720.4 and 856.8 keV transitions respectively. In fact,  $\gamma$  rays of part of this band have been reported previously, but the unfavored

states of this band (labeled with B2) had not been observed [15]. From the analysis of the present data, we obtained quite a different structure for this band compared with that found in Ref. [15]. A new unfavored sequence of  $\Delta I = 2$  transitions has been established, and three cross-link transitions have been identified and placed into the present level scheme. However, two negative-parity

states at 5111 and 6057 keV as well as the 576 keV ( $(15^-) \rightarrow 14^+$ ) and 962 keV ( $(13^-) \rightarrow 11^-$ ) transitions reported in Ref. [15] were not confirmed in the present experiment. Based on the dipole character of the 515.4, and 573.4 keV transitions and the quadrupole character

of the 638.9 keV transition, the assignments of  $I^\pi = (8^-)$  and  $(10^-)$  for the 3069.8 and 3708.7 keV levels, respectively, were proposed for sequence B2. Unfortunately, the  $R_{DCO}$  value of 723.8 keV  $\gamma$  ray cannot be deduced due to the weak intensities of the transitions.

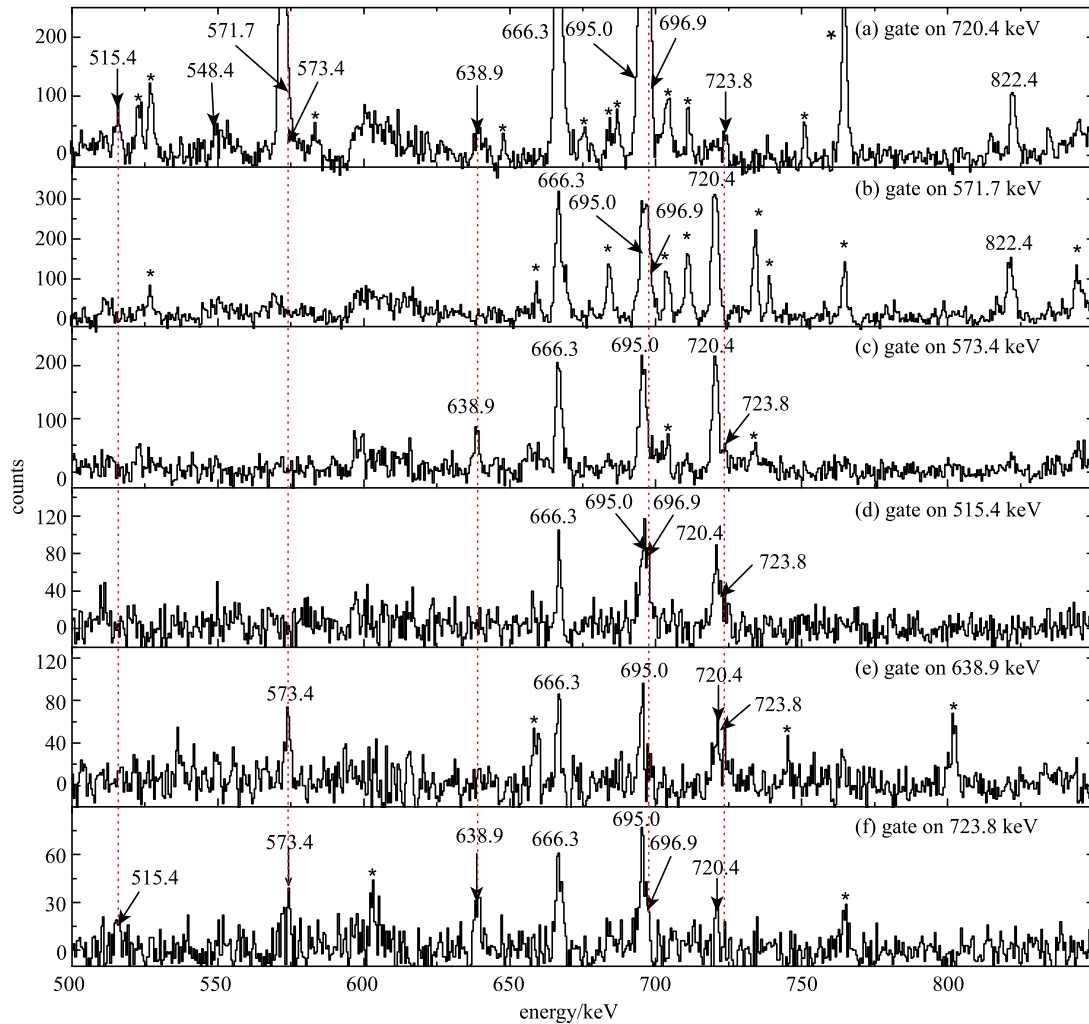


Fig. 3. (color online) Representative  $\gamma$ - $\gamma$  coincidence spectra gated on (a) 720.4, (b) 571.7, (c) 573.4, (d) 515.4, (e) 638.9, and (f) 723.8 keV transitions. The main coincidence  $\gamma$  rays are labeled with their energies in keV, while the peaks marked with asterisks are contaminants of the by-products (such as  $^{126}\text{I}$  and  $^{125}\text{Te}$ ) from the reaction.

The coincidence spectra gated on the 720.4, 571.1, 573.4, 515.4, 638.9, and 723.8 keV transitions are shown in Fig. 3 (a)-(f), from which the members of the new sequence B2, i.e., two  $\Delta I = 2$  transitions with energies of 638.9 and 723.8 keV, two newly identified cross-link transitions with energies of 573.4 and 515.4 keV, are weakly indicated. To better distinguish the newly observed  $\gamma$  rays, five red dashed lines have been placed at the energies of 515.4, 573.4, 638.9, 696.9, and 723.8 keV in the coincidence spectra as shown in Fig. 3. One can see from Fig. 3(a) that most intraband and inter-

band transitions of B1 and B2 sequences can be observed. The 573.4 and 696.9 keV transitions are easily found to be covered by the strong peaks of 571.7 and 695.0 keV transitions, respectively, with the help of the red dashed lines. As shown in Fig. 3(c) and (d), the 720.4 keV  $\gamma$  ray is the only transition of B1 that can be seen in the 573.4 keV gated spectrum, while both 720.4 and 696.9 keV  $\gamma$  rays can be observed in the 515.4 keV gated spectrum, which indicates that the 573.4 keV transition is parallel to the 696.9 keV transition, and 515.4 is parallel to the 571.7 keV transition. From Fig. 3(a) and (e), the 638.9-

keV  $\gamma$  ray is in coincidence with both 720.4 and 573.4 keV  $\gamma$  rays, while it is parallel to the 696.9 and 515.4 keV  $\gamma$  ray. It is easy to find the additive relationship of  $\gamma$  transition energies,  $638.9+573.4=515.4+696.9$ , and considering the coincidence relationships the 3708.7 keV level can be established. The intensities of the 666.3-, 695.0, 720.4, and 573.4 keV transitions are similar, as can be seen in Fig. 3(e), while the 638.9 keV  $\gamma$  ray is obviously weaker than the 666.3, 695.0, and 720.4 keV  $\gamma$  rays in the spectrum gated by the 573.4 keV transition, as shown in Fig. 3(c). This indicates that the 638.9 keV transition should be placed above the 573.4-keV transition. In Fig. 3(f), the 720.4, 696.9, 573.4, 638.9, and 515.4 keV transitions can be seen. At the same time, compared with Fig. 3(b), the 723.8 keV  $\gamma$  ray can also be weakly seen in the 720.4, 573.4, 515.4, and 638.9 keV gated spectra, respectively, as shown in Fig. 3(a), (c), (d), and (e). Therefore, the 723.8 keV  $\gamma$  ray has been placed above the 3708.7 keV level in the present level scheme.

### 3 Discussion

#### 3.1 Shape evolution and signature splitting in $^{126}\text{Te}$

The low-spin states of  $^{126}\text{Te}$  exhibit a vibrational structure, since the energy ratio  $E(4^+)/E(2^+) = 2.04$  lies close to the values for a perfect vibrator. However, the higher-spin states are characterized by quasiparticle excitations, and the opposite shape-driving effects of low- $\Omega$   $h_{11/2}$  protons and high- $\Omega$   $h_{11/2}$  neutrons lead to a variety of structures with different shapes. The high-spin region of the level scheme (see Fig. 1) is dominated by regular bands with high collectivity. Thus, the evolution from vibrational to rotational structure may occur in this nucleus as a function of spin.

In order to better understand the evolution, we employ an empirical approach to distinguish the vibrational regime from the rotational regime in atomic nuclei, called the E-GOS (a ratio of  $E_\gamma$  over spin) curve [17], which is shown in Fig. 4 for the yrast band of  $^{126}\text{Te}$ . For a vibrator, the ideal value of this ratio gradually diminishes to zero as spin increases, while for an axially symmetric rotor it rises slightly and approaches to a constant at high spins. As clearly presented in Fig. 4, the experimental E-GOS values of  $^{126}\text{Te}$  at low spin are consistent with the vibrator. Above spins of  $10\hbar$ , however, the E-GOS values do not diminish to zero and become almost constant, indicating that it may approach rotor. Thus, the E-GOS plot of the yrast band in  $^{126}\text{Te}$  indicates an evolution from a vibrational structure at lower spins to a rotational sequence above spins of  $10\hbar$ , although it shows a staggering between spins of 6–10 $\hbar$ . The likely reason for the staggering of the E-GOS plot is the competition

between the driving forces of protons and neutrons.

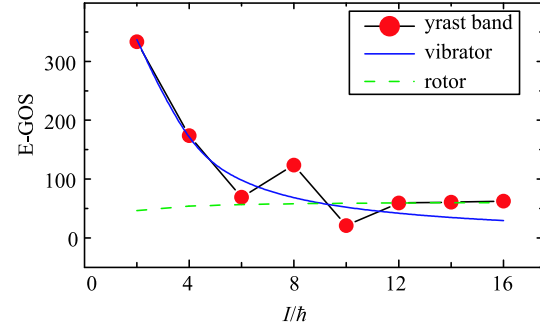


Fig. 4. (color online) The E-GOS curve of the yrast band in  $^{126}\text{Te}$ , together with predictions of the vibrator (blue line).

Signature is the quantum number associated with the rotation of a deformed nucleus around a principal axis by  $180^\circ$ . Due to this symmetry, rotational energies  $E(I)$  of a high- $j$  band can be split into two branches with  $\Delta I = 2$  and classified by the signature quantum number,  $\alpha$ . As a rule,  $\alpha$  is 0 or 1 for a system with integer spin and  $-1/2$  or  $1/2$  for a system with half-integer spin. Signature splitting is a sensitive probe of deformation. In particular, it indicates triaxial deformation, as is discussed in the following. The energy staggering in the form of  $\Delta E = E(I) - [E(I+1) + E(I-1)]/2$  for negative-parity band in  $^{126}\text{Te}$  is plotted in Fig. 5. It can be seen from Fig. 5 that the signature splitting is large and almost constant within the entire observed spin range.

The above experimental phenomena will be analyzed within the framework of the CNS and CNSB models.

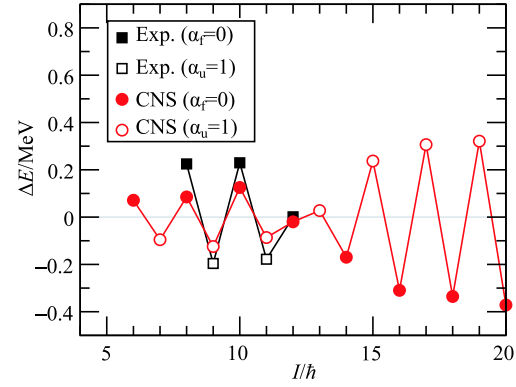


Fig. 5. (color online) The CNS and experimental signature splittings of the negative parity bands in  $^{126}\text{Te}$ . The solid and open symbols indicate  $\alpha = 0$  and  $\alpha = 1$  sequences respectively.

#### 3.2 CNS and CNSB model calculations

The CNS model has been highly successful in describing high-spin rotational structures across the whole nuclear chart [18, 19]. The virtual interaction between the

Routhians are removed then the single particle Routhians are connected diabatically with respect to rotating frequencies. A sum of the rotating liquid drop energy and shell energy corrections calculated by the Strutinsky procedure [20] gives the total nuclear energy at specified deformation and spin. The neglecting of pairing has an advantage in that the tracing of a fixed configuration undergoing drastic deformation changes becomes possible over the considerable spin range up to the band termination. The CNSB model [21, 22] has further included the pairing correlations. The total energy after the particle number projection (PNP) is minimized not only in deformation space but also in a mesh of the pairing parameters, Fermi energy  $\lambda$  and pairing gap  $\Delta$ . However, by introducing the pairing correlations, the wave functions of the orbitals near the Fermi levels are largely mixed. The nucleon number in the high- $j$  shell is no longer conserved. That makes it impossible to trace a configuration reliably in a deformation mesh, thus usually only the yrast bands are given.

On the basis of Nilsson orbitals, the ground state positive parity band A of  $^{126}\text{Te}$  is built upon the configuration of  $\pi(1g_{7/2}2d_{5/2})^2 \otimes \nu(2d_{5/2}1g_{7/2}3s_{1/2})^1(h_{11/2})^8$  relative to  $^{100}\text{Sn}$ . In the following, this band is discussed in the framework of the CNSB model, as the pairing correlations play a significant role in the rotational structure of even-even  $^{126}\text{Te}$  before the first backbending. The negative parity band B of  $^{126}\text{Te}$  is built by exciting one neutron from the  $h_{11/2}$  to  $N = 4$  low- $j$  shell. Because the signature splittings of the high- $\Omega$   $h_{11/2}$  and  $N = 4$  low- $j$  shell are small, two configurations with the same number of neutrons in these two shells and the same combined parity and signature have similar energies. Thus it is necessary to distinguish between the high- $j$  and low- $j$  orbitals, therefore we have to turn to the CNS approach in the discussion of the negative parity band.

Both the CNSB and CNS calculations were carried out in a quadrupole and hexadecapole deformation mesh ( $\varepsilon_2, \gamma, \varepsilon_4$ ) with the  $A \sim 130$  Nilsson parameters [18, 23]. Total energies are calculated as the sum of the rotating liquid-drop energy ( $E_{\text{rld}}$ ) and the shell energy using the Strutinsky method [24, 25]. The Lublin-Strasbourg drop (LSD) model [26] is used for the static liquid-drop energy. The rigid-body moments of inertia are calculated with a radius parameter of  $r_0 = 1.16$  fm and a diffuseness of  $a = 0.6$  fm [27]. The calculations minimize the energies for different configurations and for different spins with respect to the deformation parameters ( $\varepsilon_2, \gamma, \varepsilon_4$ ).

### 3.2.1 Positive parity band

The CNSB results are compared with the experimental energies in Fig. 6. It is seen that the experimental data of the positive parity band are fairly well reproduced. Selected examples of potential energy surfaces (PESs) for the  $(+,0)(+,0)$  configuration are presented in Fig. 7.

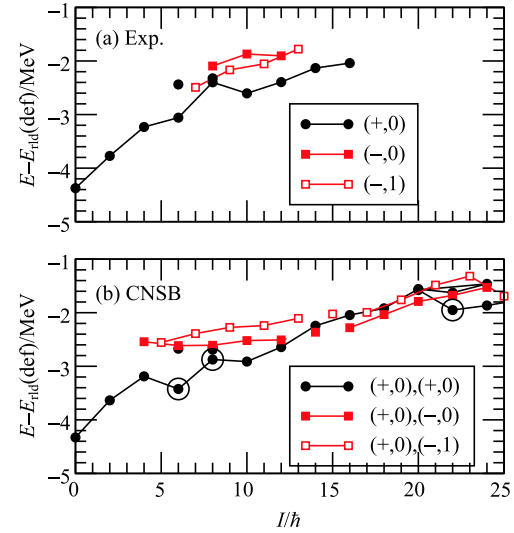


Fig. 6. (color online) The experimental and CNSB rotating energies in  $^{126}\text{Te}$ . The theoretical bands are labeled by the combination of parity and signature of protons and neutrons  $(\pi_p, \alpha_p)(\pi_n, \alpha_n)$ . The noncollective states are indicated by large open circles.

For low spins in  $^{126}\text{Te}$ , two valence protons have the capability to drive the nucleus to a prolate shape, while the neutron  $gsd$  and  $h_{11/2}$  shells are over half-filled, so the valence neutrons tend to drive the nucleus to an oblate shape. The competition between the proton and neutron driving forces results in a soft shape, which can be seen from the PESs in Fig. 7. The first aligned state at  $I^\pi = 6^+$  is built by the alignment of two valence protons in  $\pi[(g_{7/2}, d_{5/2})]$ . This state is seen in the experimental level scheme at 1776.0 keV with rather long lifetime. The collective  $I^\pi = 6^+$  state is 0.81 MeV higher than the fully aligned state in the calculations. In the experimental level scheme the  $6_2^+$  state was also observed and is 0.62 MeV higher than  $6_1^+$  state. As for the  $I^\pi = 8^+$  states, three competitive minima appear in the PES, with one aligned state at  $\gamma = -120^\circ$  and two triaxial states at  $\gamma \sim 30^\circ$  and  $-45^\circ$ , respectively. The aligned state at  $\gamma = -120^\circ$  is built by breaking one  $h_{11/2}$  neutron pair, i.e. by exciting one  $m = -7/2$  neutron to the  $m = 9/2$  orbital. For  $I \geq 10\hbar$  where two  $h_{11/2}$  quasi-neutrons (mainly  $[523]7/2$  components) are aligned, the collective positive parity band prefers a triaxial shape and rotates around the intermediate axis.

It is noted that the experimentally observed yrast  $I^\pi = 16^+$  states in even-mass Te isotopes with  $114 \leq A \leq 122$  have been interpreted as favored noncollective oblate states based on the fully aligned  $\pi[(g_{7/2}d_{5/2})^2]_{6+} \otimes \nu[(h_{11/2})^2]_{10+}$  configuration [28]. Furthermore, it is also pointed out in Ref. [28] that the  $(16^+)$  state in  $^{124}\text{Te}$  does not exhibit the characteristics of the favored noncollective oblate states with  $I^\pi = 16^+$  observed in the lighter

doubly even Te isotopes. In the CNSB calculations the oblate  $16^+$  state is strongly favored in  $^{120}\text{Te}$ , only slightly favored in  $^{122}\text{Te}$  and clearly the collective minimum is the favored one in  $^{124,126}\text{Te}$ . Our calculations confirm the prospect suggested in Ref. [28] that the  $16^+$  in  $^{124}\text{Te}$  is no longer an aligned state but a collective rotating one. Another fully aligned state is predicted at spin  $I = 22\hbar$  as shown in Fig. 6, which can be explained by coupling the protons in  $\pi(g_{7/2}, d_{5/2})$  orbitals with  $I_{\max}^\pi = 6^+$  to a neutron configuration with  $I_{\max}^\pi = 16^+$ . Our calculations also show that the  $22^+$  state is expected to be the corresponding aligned state to the  $22^+$  state observed in  $^{120}\text{Te}$  [3]. Unfortunately, this state could not be observed in the present experiment.

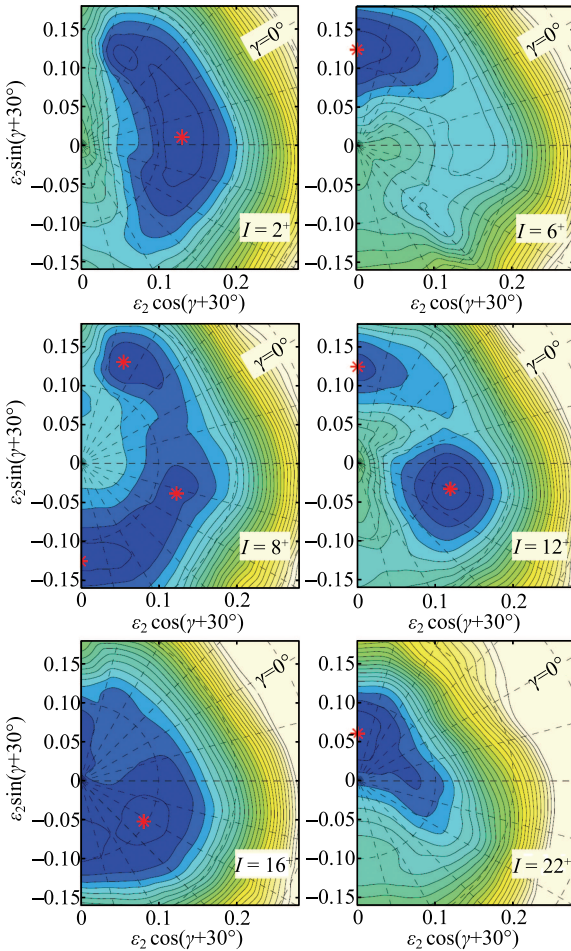


Fig. 7. (color online) The potential energy surface of the calculated  $(+,0),(+,0)$  states in  $^{126}\text{Te}$ . The energy difference between neighboring equipotential lines is 0.25 MeV. The minima in the PES are marked with asterisks.

### 3.2.2 Negative parity band

Figure 6 also shows the calculated energies of negative-parity bands compared with the experimental data. The general trend of  $E - E_{\text{rld}}$  is well reproduced

by the CNSB calculations. However, the phase of signature splittings are inconsistent between the CNSB and experimental results. The  $\alpha = 1$  branch is favored in the experimental level scheme while it is opposite in the CNSB calculations. As we have stated in the second paragraph of Section 3.2, the unpaired orbitals of the signature partner have somewhat small signature splittings, therefore two configurations with the same combined parity and signature but with different numbers of nucleons in high- $j$  and low- $j$  shells will have similar energies.

In order to do such calculations, the CNS model, which does not take account of the pairing correlations, is used. The pairing correlations play a minor role as far as only the signature splitting is concerned. In Fig. 8, the CNS rotational energies are compared with the experimental results. The energy differences of the negative parity bands, shown in Fig. 8(c), follow a similar trend to the positive parity band, and drop with increasing spin. In Fig. 8(b), it is seen that the  $\nu(\text{gsd})_{\pm 1/2}^{17}(h_{11/2})_{1/2}^7$  is lower in energy at low spins while  $\nu(\text{gsd})_{\pm 1/2}^{17}(h_{11/2})_{-1/2}^7$  is more favored at high spins. From the experimental point

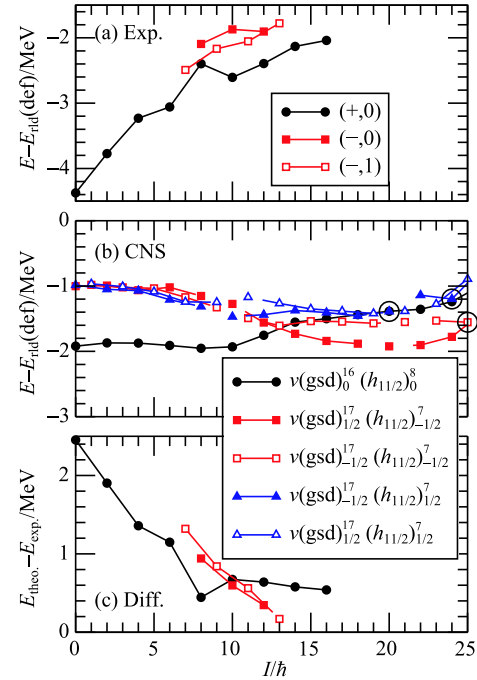


Fig. 8. (color online) Comparison between the (a) experimental rotational energies and (b) CNS, with rigid rotor references subtracted. Their differences are shown in (c). In (a), the experimental results are labeled by the combination of parity and signature. In (b), the theoretical results are labeled respectively by their neutron configurations with the occupation number in each shell as the superscript and the signature as the subscript. The proton configuration is the same with two valence protons in the  $h_{11/2}$  shell.

of view, it is preferable to follow the decay path of the latter configuration. More importantly, the favored shape of the  $\nu(\text{gsd})_{\pm 1/2}^{17}(h_{11/2})_{-1/2}^7$  configuration goes through a change from a triaxial shape with  $\gamma \sim -45^\circ$  for  $I \geq 12^-$  to a triaxial shape with  $\gamma \sim 30^\circ$  at lower spins. The change of shape results in a flip-flop in the favored signature for the negative parity band B. With such interpretation, the experimental energy staggerings, defined as  $\Delta E = E(I) - [E(I+1) + E(I-1)]/2$ , can be reasonably well reproduced, as shown in Fig. 5.

## 4 Summary

In summary, high-spin states in the nucleus  $^{126}\text{Te}$  were populated via the reaction  $^{124}\text{Sn}(^7\text{Li}, 1\text{p}4\text{n})^{126}\text{Te}$ . The level scheme of  $^{126}\text{Te}$  has been enriched by adding seven new  $\gamma$  rays and a new negative-parity sequence has been established. CNSB and CNS calculations were carried out to better understand the structure of the

observed bands. The PESs calculations for the yrast band structures show a shape competition between triaxial shape and collective oblate shape. In particular, three competitive minima appear in the potential energy surface for the  $I^\pi = 8^+$  states, with one aligned state at  $\gamma = -120^\circ$  and two triaxial states at  $\gamma \sim 30^\circ$  and  $-45^\circ$ , respectively. Band B shows a large signature splitting, and the configuration of this negative parity band is assigned as  $\nu(\text{gsd})_{\pm 1/2}^{17}(h_{11/2})_{\pm 1/2}^7$ . The favored shape of the  $\nu(\text{gsd})_{\pm 1/2}^{17}(h_{11/2})_{-1/2}^7$  configuration goes through a change from a triaxial shape with  $\gamma \sim -45^\circ$  for  $I \geq 12^-$  to a triaxial shape with  $\gamma \sim 30^\circ$  at lower spins. The change of shape results in an inversion in the favored signature for the negative parity band.

*The authors would like to thank the crew of the HI-13 tandem accelerator at the China Institute of Atomic Energy for steady operation of the accelerator and for preparing the target.*

## References

- 1 Y. Liang, R. Ma, E. S. Paul et al, Phys. Rev. Lett., **64**: 29 (1990)
- 2 A. Granderath, P. Mantica, R. Bengtsson, et al, Nuclear Physics A, **597**: 427 (1996)
- 3 S. Nag, A. K. Singh, A. N. Wilson et al, Phys. Rev. C, **85**: 014310 (2012)
- 4 N. Xu, J.-Y. Zhang, Y. Liang, R. Ma et al, Phys. Rev. C, **42**: 1394 (1990)
- 5 Y. Liang, D. B. Fossan, J. R. Hughes et al, Phys. Rev. C, **45**: 1041 (1992)
- 6 K. Selvakumar, A. K. Singh, S. Das et al, Phys. Rev. C, **88**: 024313 (2013)
- 7 F. R. Xu, P. M. Walker, and R. Wyss, Phys. Rev. C, **59**: 731 (1999)
- 8 Y. S. Chen, S. Frauendorf, and G. A. Leander, Phys. Rev. C, **28**: 2437 (1983)
- 9 P. J. Nolan, R. Aryaeinejad, P. J. Bishop et al, Journal of Physics G: Nuclear Physics, **13**: 1555 (1987)
- 10 J. R. Vanhoy, J. A. Tanyi, K. A. Crandell et al, Phys. Rev. C, **69**: 064323 (2004)
- 11 T. von Egidy, C. Doll, J. Jolie et al, Nuclear Physics A, **714**: 355 (2003)
- 12 J. Ott, C. Doll, T. von Egidy et al, Nuclear Physics A, **625**: 598 (1997)
- 13 A. Kerek, Nuclear Physics A, **176**: 466 (1971)
- 14 C. Zhang, P. Bhattacharyya, P. Daly et al, Nuclear Physics A, **628**: 386 (1998)
- 15 A. Astier, M.-G. Porquet, T. Venkova et al, The European Physical Journal A, **50**: 2 (2014)
- 16 D. Radford, Nuclear Instruments and Methods in Physics Research Section A: Accelerators, Spectrometers, Detectors and Associated Equipment, **361**: 297 (1995)
- 17 P. H. Regan, C. W. Beausang, N. V. Zamfir et al, Phys. Rev. Lett., **90**: 152502 (2003)
- 18 A. Afanasjev, D. Fossan, G. Lane and I. Ragnarsson, Physics Reports, **322**: 1 (1999)
- 19 B. G. Carlsson and I. Ragnarsson, Phys. Rev. C, **74**: 011302 (2006)
- 20 V. Strutinsky, Nuclear Physics A, **95**: 420 (1967)
- 21 B. G. Carlsson, I. Ragnarsson, R. Bengtsson et al, Phys. Rev. C, **78**: 034316 (2008)
- 22 H.-L. Ma, B. G. Carlsson, I. Ragnarsson and H. Ryde, Phys. Rev. C, **90**: 014316 (2014)
- 23 J.-Y. Zhang, N. Xu, D. B. Fossan et al, Phys. Rev. C, **39**: 714 (1989)
- 24 G. Andersson, S. Larsson, G. Leander et al, Nuclear Physics A, **268**: 205 (1976)
- 25 V. Strutinsky, Nuclear Physics A, **122**: 1 (1968)
- 26 K. Pomorski and J. Dudek, Phys. Rev. C, **67**: 044316 (2003)
- 27 B. G. Carlsson and I. Ragnarsson, Phys. Rev. C, **74**: 044310 (2006)
- 28 N. Fotiades, J. A. Cizewski, R. Krücken et al, Phys. Rev. C, **89**: 017303 (2014)